ADVANCED MATERIALS
www.advmat.de

Observation of Antiferroelectric Domain Walls in a Uniaxial Hyperferroelectric

Michele Conroy, Didrik René Småbråten, Colin Ophus, Konstantin Shapovalov, Quentin M. Ramasse, Kasper Aas Hunnestad, Sverre M. Selbach, Ulrich Aschauer, Kalani Moore, J. Marty Gregg, Ursel Bangert, Massimiliano Stengel, Alexei Gruverman,* and Dennis Meier**

Ferroelectric domain walls are a rich source of emergent electronic properties and unusual polar order. Recent studies show that the configuration of ferroelectric walls can go well beyond the conventional Ising-type structure. Néel-, Bloch-, and vortex-like polar patterns have been observed, displaying strong similarities with the spin textures at magnetic domain walls. Here, the discovery of antiferroelectric domain walls in the uniaxial ferroelectric $Pb_5Ge_3O_{11}$ is reported. Highly mobile domain walls with an alternating displacement of Pb atoms are resolved, resulting in a cyclic 180° flip of dipole direction within the wall. Density functional theory calculations show that $Pb_5Ge_3O_{11}$ is hyperferroelectric, allowing the system to overcome the depolarization fields that usually suppress the antiparallel ordering of dipoles along the longitudinal direction. Interestingly, the antiferroelectric walls observed under the electron beam are energetically more costly than basic head-to-head or tail-to-tail walls. The results suggest a new type of excited domain-wall state, expanding previous studies on ferroelectric domain walls into the realm of antiferroic phenomena.

1. Introduction

Lead germanate, $Pb_5Ge_3O_{11}$, is a uniaxial ferroelectric material with a spontaneous polarization P_S = 4.8 μC cm^{-2} along the crystallographic [001] direction and an enantiomorphic structure (space group *P*3).[1,2] One of the most peculiar consequences of the enantiomorphism in $Pb_5Ge_3O_{11}$ is its polarization-dependent optical activity, which makes ferroelectric 180° domains discernible in polarized light.[2,3] Because of the unipolar structure of $Pb_5Ge_3O_{11}$, only 180° domains exist in this material, forming irregular patterns elongated along the polar [001] axis as shown in **Figure 1a**. An interesting feature of the associated domain walls is that they can be strongly inclined with respect to the polar axis, giving rise to head-to-head and

M. Conroy
Department of Materials
London Centre of Nanotechnology
Imperial Henry Royce Institute
Imperial College London
London SW7 2AZ, UK
E-mail: mconroy@imperial.ac.uk

D. R. Småbråten[+], K. A. Hunnestad, S. M. Selbach, D. Meier
Department of Materials Science and Engineering
NTNU Norwegian University of Science and Technology
Trondheim 7491, Norway
E-mail: dennis.meier@ntnu.no

D. R. Småbråten[+], U. Aschauer
Department of Chemistry, Biochemistry and Pharmaceutical Sciences
University of Bern
Bern CH-3012 Bern, Switzerland

The ORCID identification number(s) for the author(s) of this article can be found under https://doi.org/10.1002/adma.202405150

[+]Present address: Department of Sustainable Energy Technology, SINTEF Industry, P.O. Box 124 Blindern, Oslo NO-0373, Norway

C. Ophus
National Center for Electron Microscopy
Molecular Foundry
Lawrence Berkeley National Laboratory
Berkeley, CA 94720, USA

K. Shapovalov, M. Stengel
Institut de Ciencia de Materials de Barcelona (ICMAB-CSIC)
Campus UAB
Bellaterra 08193, Spain

K. Shapovalov
Theoretical Materials Physics, Q-MAT
University of Liège
B-4000 Sart-Tilman, Liège, Belgium

Q. M. Ramasse
School of Physics and Astronomy
School of Chemical and Process Engineering
University of Leeds
Leeds LS2 9JT, UK

Q. M. Ramasse
SuperSTEM
SciTech Daresbury Science and Innovation Campus
Daresbury WA4 4AD, UK

U. Aschauer
Department of Chemistry and Physics of Materials
University of Salzburg
Salzburg 5020, Austria

DOI: 10.1002/adma.202405150

tail-to-tail sections with unusual electronic and dynamical responses. For example, the nominally charged domain walls have been reported to form characteristic saddle points that remove the need for screening charges[4] and scanning probe experiments showed that they expand in length under application of an electric field.[5] These physical properties are incompatible with the formation of classical Ising-type walls, pointing toward a more complex domain wall structure. In this study, we use density functional theory (DFT) calculations to understand the microscopic origin of the ferroelectric polarization in $Pb_5Ge_3O_{11}$ and apply different scanning transmission electron microscopy (STEM) methods to resolve the atomic-scale structure of the nominally charged domain walls.

2. Results and Discussion

2.1. Hyperferroelectriciy in $Pb_5Ge_3O_{11}$

We begin by analyzing the structural instabilities of the prototypical centrosymmetric bulk phase (space group $P\bar{6}$) that drive the ferroelectric order in $Pb_5Ge_3O_{11}$. Our DFT calculations reveal a single discontinuous unstable phonon band at the center of the Brillouin zone (Figure S1a, Supporting Information), consistent with the system's uniaxial ferroelectricity and the associated reduction in space group symmetry ($P\bar{6} \rightarrow P3$). Interestingly, by comparing the ferroelectric and prototypical structures (phonon analysis performed with AMPLIMODES[6]), we find that both a polar (Γ_2) and a non-polar mode (Γ_1) are involved in the ferroelectric phase transition (Movie S1 and Figure S2, Supporting Information present a visualization of the Γ_1 and Γ_2 modes). The corresponding 2D potential energy landscape is given in Figure 1b with cell parameters fixed to those of the ferroelectric structure. These results show that the ferroelectric ground state is not stabilized by condensing the polar Γ_2 mode, but becomes stable only when both the polar and non-polar modes condense, analogous to an improper ferroelectric phase transition.[7,8] We further find that the elastic energy (obtained by comparison with the lattice parameters of the prototypical phase) is significantly smaller than the phonon mode condensation, suggesting that contributions from macroscopic elasticity are minor. Following the symmetry of the prototypical phase, the coupling of the polar and non-polar modes at leading order in the amplitude is of the type $\Gamma_2{}^2\Gamma_1$. Based on the ab-initio calculations, we construct a minimal Landau model of the potential energy landscape $F(\Gamma_1,\Gamma_2)$ as presented in Figure 1c, showing two minima as function of Γ_2 that correspond to the two ferroelectric domain states with $+P$ and $-P$ (see Note S1, Supporting Information for details). To describe the effect of the depolarizing electric fields, we plot the potential energy, including the electrostatic energy ($F(\Gamma_1,\Gamma_2)+F_{el}$), as a function of the electric displacement field D[9], regarding D as an external parameter (Figure 1d). The resulting curve is very different from the double-well potential of classical proper ferroelectrics. The main difference is the emergence of a bi-stable state in open-circuit conditions ($D = 0$) with a nonzero polarization, whereas the unstable prototypical structure lies at substantially higher energy. This behavior identifies $Pb_5Ge_3O_{11}$ as a uniaxial hyperferroelectric material,[10] where the polar instability survives under longitudinal (in addition to transverse) open-circuit electrical boundary conditions (Figure S1, Supporting Information). Thus, in contrast to classical proper ferroelectrics, where depolarizing fields completely suppress the ferroelectric instability in open-circuit conditions, $Pb_5Ge_3O_{11}$ sustains its ferroelectric order for $D = 0$. Simultaneously with our study, hyperferroelectricity in $Pb_5Ge_3O_{11}$ was independently confirmed in ref. [11] with a similar energy landscape $F(\Gamma_1,\Gamma_2)$ as reported in ref. [12]; it was also shown in these works that spin-orbit coupling further increases the stability of the ferroelectric phase in both short-circuit and open-circuit electrical boundary conditions. Most importantly for our work, in principle, the hyperferroelectricity enables atomically sharp charged domain walls (head-to-head and tail-to-tail) even in the absence of mobile screening carriers as previously discussed for $LiNbO_3$,[13,14] making it largely immune against the emergence of uncompensated bound charges.

2.2. Polar displacements in $+P$ and $-P$ domains

To measure the domain wall structure in $Pb_5Ge_3O_{11}$, we image the polar order at the atomic scale using different STEM experiments. The STEM images in **Figure 2**a–c delineate the domain configuration on the non-polar (010) surface, where the polarization direction within the field of view was determined by STEM differential phase contrast (DPC) (see Experimental Section and Figures S3 and S4, Supporting Information).[15–17] Here, dark and bright areas correspond to $+P$ and $-P$ domains, respectively, revealing an extended tail-to-tail domain wall with a sawtooth-like structure. The image series shows that the tail-to-tail domain wall is remarkably mobile, changing position from frame to frame, which we attribute to an interaction with the electron probe (Movie S2, Supporting Information).[16,18,19] The same behavior is observed in large-area scans obtained by scanning electron microscopy (SEM), independent of the scan direction of the SEM probe (Figure S4, Supporting Information).

K. Moore
Direct Electron LP
San Diego, CA 92128, USA
J. M. Gregg
Centre for Quantum Materials and Technologies
School of Mathematics and Physics
Queen's University Belfast
Belfast BT7 1NN, UK
U. Bangert
Department of Physics
Bernal Institute
University of Limerick
Limerick V94 T9PX, Ireland
M. Stengel
Institució Catalana de Recerca i Estudis Avançats (ICREA)
Pg. Lluís Companys
Barcelona 08010, Spain
A. Gruverman
Department of Physics and Astronomy
Nebraska Center for Materials and Nanoscience
University of Nebraska
Lincoln, NE NE 68588, USA
E-mail: agruverman2@unl.edu

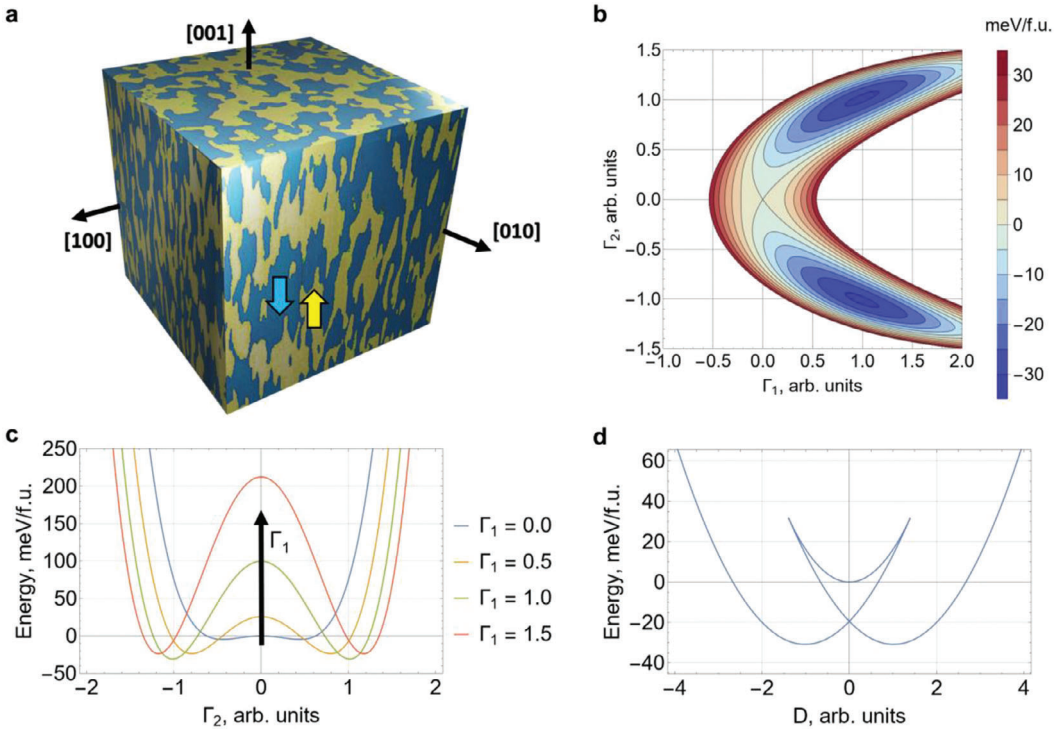

Figure 1. Domain structure and free energy landscape of $Pb_5Ge_3O_{11}$. a, 3D sketch of the as-grown domain structure constructed based on piezoresponse force microscopy measurements. b, Contour plot of the 2D potential energy landscape with respect to non-polar Γ_1 and polar Γ_2 mode amplitudes as extracted from ab-initio calculations. c, Ferroelectric double-well potential for different non-polar mode amplitudes Γ_1. d, Plot of the potential energy versus displacement field, D, showing the hyperferroelectric behavior of the material with three possible polar states. The minima at $D = \pm 1$ correspond to the two polar states $+P$ and $-P$ ($E = -30$ meV f.u.$^{-1}$), which remain stable in open-circuit conditions ($D = 0$, $E = -20$ meV f.u.$^{-1}$). The local minimum at $D = 0$ corresponds to the non-polar prototype phase ($E = 0$ meV f.u.$^{-1}$).

Corresponding high-resolution annular dark-field (ADF) STEM images recorded along the [010] and [100] zone axes are shown in Figure 2d,e, respectively, presenting the atomic structure, which is consistent with earlier neutron diffraction studies.[20] $Pb_5Ge_3O_{11}$ contains layers of isolated tetrahedra (GeO_4) and layers of double tetrahedra (Ge_2O_7); the Pb atoms are located in threefold triangular pyramids and sixfold triangular prisms. The spontaneous polarization is associated with a displacement of Pb atoms located in triangular prisms along the [001] direction, resulting in distinct Pb plane spacings (d_1, d_2, and d_3) as illustrated in the unit cell images in Figure 2d,e. In $+P$ ($-P$) domains, three of the sixfold coordinated Pb atoms in the unit cell move upwards (downwards), leading to a shorter (longer) distance d_1 compared to d_2, whereas d_3 remains constant (see also Figure S5, Supporting Information). Quantifying the Pb plane spacings for a $-P$ domain, we find $d_1 = 3.462$ Å $\pm$ 0.021 Å, $d_2 = 3.417$ Å $\pm$ 0.025 Å, and $d_3 = 3.771$ Å $\pm$ 0.025 Å. The relative change in Pb column positions, as well as the positions of light oxygen atoms relative to heavier Pb and Ge atomic columns (see Figures S6 and S7, Supporting Information), are in qualitative agreement with the reported ferroelectric structure of $Pb_5Ge_3O_{11}$[20] and our DFT results (Figure S8, Supporting Information). We note that quantitatively, however, the difference between d_1 and d_2 measured based on the ADF STEM is much smaller compared to the calculated values and previous experimental results.

2.3. Antiferroelectric domain walls

After characterization of the $+P$ and $-P$ domains, we next turn to the nominally charged domain walls. We find that bright field transmission electron microscopy (TEM) imaging at low dose and low magnification reduces effects from domain wall motion, showing a region of reduced intensity between $+P$ and $-P$ domains with a width $\gtrsim$16 nm (Figure S9, Supporting Information). This value is substantially larger than what is expected for a domain wall in a hyperferroelectric system[13,14] and also much larger than for 180° domain walls in conventional perovskite-type ferroelectrics, which have a typical width of ≈5–10 Å.[21,22] The large width prohibits imaging of the entire region of interest in a single STEM frame with spatial resolution and signal-to-noise ratio per atomic column sufficient for atomic displacement mapping. To overcome this experimental challenge, we perform high-resolution ADF STEM imaging separately on both sides of the low-intensity region associated with the domain wall as shown in **Figure 3**a,b (see Experimental Section for details). The ADF STEM imaging demonstrates that a distinct stripe-like pattern arises in connection with the tail-to-tail domain wall, which distinguishes it from the $+P$ (Figure 3a) and $-P$ (Figure 3b) domains with homogeneous polarization orientation. This stripe-like pattern is observed for different polarization configurations as shown in Figure S10 (Supporting Information), suggesting that it arises in association with both tail-to-tail and head-to-head

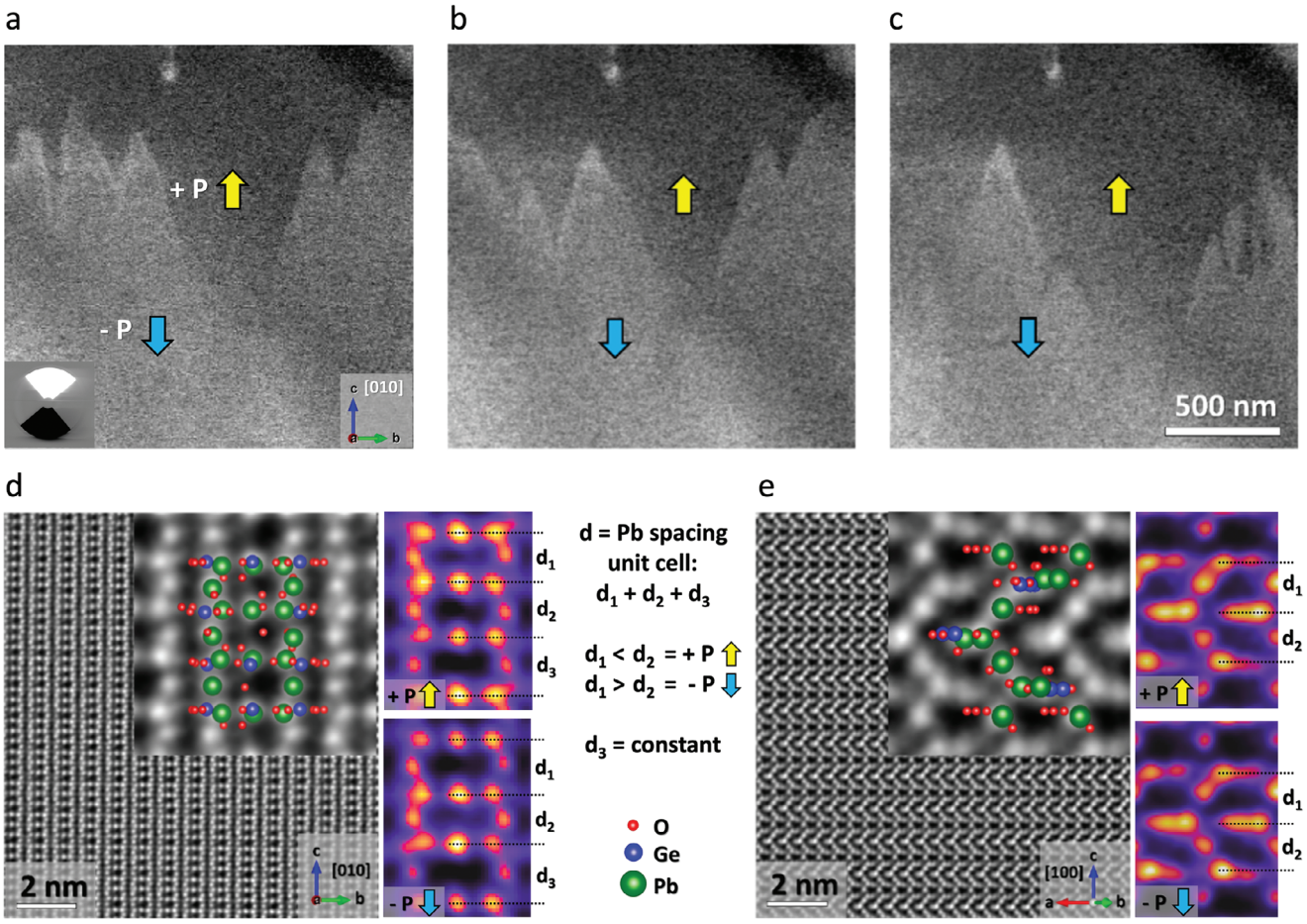

Figure 2. Polar structure of $Pb_5Ge_3O_{11}$. a–c, STEM DPC maps recorded in consecutive frames, showing antiparallel 180° domains (+*P* dark, −*P* bright). The position of the domain walls varies between the three images, showing that the walls are highly mobile, moving under electron beam irradiation. The inset image of the quadrant ADF detector to a shows that the lower quadrant was subtracted from the upper to create the images a–c. Yellow and blue arrows indicate the polarization directions in +*P* and -*P* domains. d, Representative ADF STEM image of the atomic structure viewed along the [010] direction. The inset shows the atomic model of the unit cell, overlaid on a magnified section of the image.[20] The colorized ADF STEM panels on the right in **d** display the Pb spacing of unit cells associated with positive (+*P*, top) and negative (−*P*, bottom) polarization, parametrized by d_1, d_2, and d_3. e, Same as in **d** recorded along the [100] zone axis.

domain walls. The stripe-like pattern is more readily illustrated using Fourier filtering, as shown in the processed Fourier-filtered image in Figure 3c (see Figure S11, Supporting Information and ref. [23] for details). Importantly, as the stripe-like pattern is not observed within +*P* and −*P* domains, we can exclude that it is caused by the electron probe alone and that it requires the presence of a domain wall to emerge.

We then map the atomic displacements as explained in the Experimental Section and fingerprint the local polarization as shown in Figure 3d–f (see Figure S12, Supporting Information for source images and details). We find that the atomic structure of the domain walls typically exhibits three characteristic regions. Starting from the −*P* domain in Figure 3b with uniform orientation of the electric dipoles (Figure 3d), the atomic structure transforms into an aperiodic pattern of dipole alignment formed by unit cells with limited short-range ordering of the alternating Pb displacements (Figure 3e). Subsequently, this aperiodic pattern evolves into a well-defined structure with periodically changing directions of Pb displacements, forming a regular antiparallel dipole alignment (Figure 3f). We note that this type of structural transformation is independent of the viewing direction and wall type (i.e., it is also seen at head-to-head domain walls) and can be observed in the images recorded along the [010] and [100] directions (Figure S10, Supporting Information). Based on the STEM data, we conclude that toward the center of nominally charged tail-to-tail and head-to-head domain walls, the ferroelectric order transforms into an antipolar structure, corresponding to antiferroelectrically coupled dipole layers (Figure 3g), for which the direction of *P* changes from one layer to the next.

2.4. (Meta)stability of the antiferroelectric order

The observation of antiparallel dipoles within the tail-to-tail and head-to-head walls is consistent with the robustness of $Pb_5Ge_3O_{11}$ against the emergence of domain wall bound charges as expected due to its hyperferroelectric nature. However, although hyperferroelectricity enables the formation of such

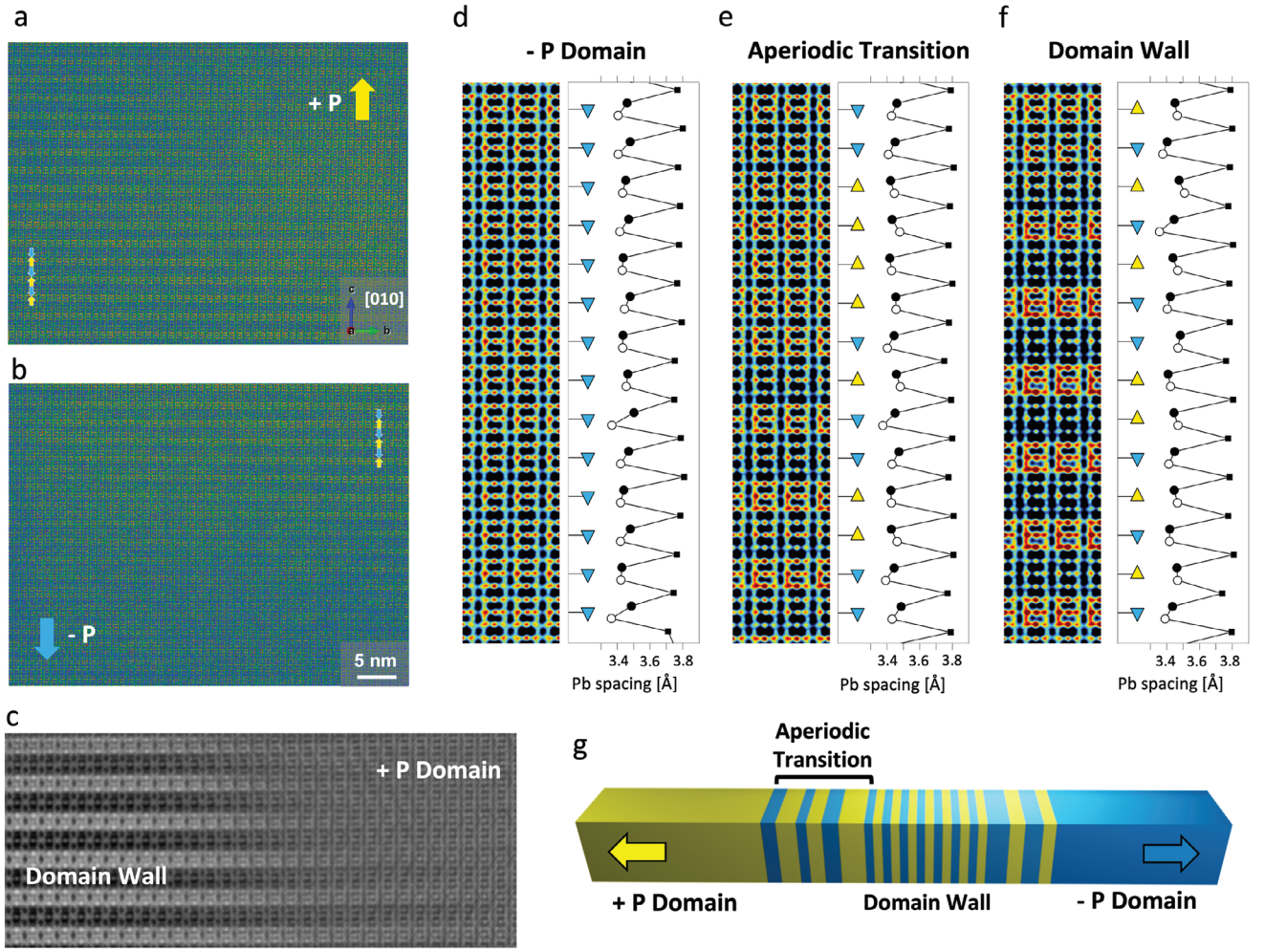

Figure 3. Atomic-scale structure of domain walls in $Pb_5Ge_3O_{11}$. a,b, ADF STEM imaging of $+P$ (a) and $-P$ (b) domain regions transitioning into antipolar regions; imaged along the [010] direction. c, Fourier-filtered image (selecting the superlattice spots) of a section of the ADF STEM image in a, highlighting the stripe-like pattern associated with the tail-to-tail domain wall. d–f, ADF STEM maps along with the corresponding cell-to-cell dipole alignments arising due to the displacement of the Pb atoms. d, $+P$ domain region, e, aperiodic transition region, f, domain wall. Black and white circles correspond to the measured atomic spacing of the Pb atoms in the triangular prisms in the [001] direction. Black squares correspond to the unshifted Pb atoms in the triangular pyramids. Yellow and blue arrowheads denote the resulting $+P$ and $-P$ polarizations based on the inter-layer distances d_i (i = 1,2,3) as defined in Figure 2 ($+P$: $d_1 < d_2$; $-P$: $d_1 > d_2$). g, Schematic illustration of the dipole layer-by-layer alignment corresponding to the atomic structure in d to f.

atomically sharp antiparallel polar segments,[13] it cannot explain the short-period modulation observed experimentally. To understand the energetics of the emergent antiferroelectric order, we revisit the phonon dispersion of the prototypical phase ($P\bar{6}$, see Figure S1a, Supporting Information). We find an unstable antiferroelectric phonon mode (A_1, modulation q = (0, 0, ½)) with an imaginary frequency comparable to Γ_2, that is structurally consistent with the antiferroelectric order observed experimentally at the domain walls. Static mapping of the energy as a function of the A_1 phonon amplitude (Figure S1b,c, Supporting Information) reveals that the antiferroelectric instability results in a small energy lowering relative to the prototypical phase. Starting from the A_1 structure close to the energy minimum in Figure S1c (Supporting Information), we find a total energy lowering of the antiferroelectric (AFE) phase relative to the prototype phase of $\Delta E(\text{AFE}) = 3$ meV f.u.$^{-1}$ after full structural relaxation, suggesting that the antiferroelectric phase is (meta)stable in $Pb_5Ge_3O_{11}$. This is further confirmed by the lack of unstable phonon modes in the phonon dispersion of the antiferroelectric structure after relaxation (Figure S13, Supporting Information). Investigating the resulting atomic configuration after full relaxation more closely, we find that the atomic displacement of the central Pb atoms (Figure S14, Supporting Information), which gives rise to the alternating dipole alignment, persists after structural relaxation, providing additional evidence for the (meta)stability of antiferroelectric order.

From the point of view of atomic displacements, the Γ mode (Figure S14a,b, Supporting Information) of the antiferroelectric phase is almost identical to the non-polar Γ_1 mode of the ferroelectric phase (Figure S15a,b, Supporting Information). In the A-point distortion, the lower half, as depicted in Figure S14d (Supporting Information), has the opposite displacement

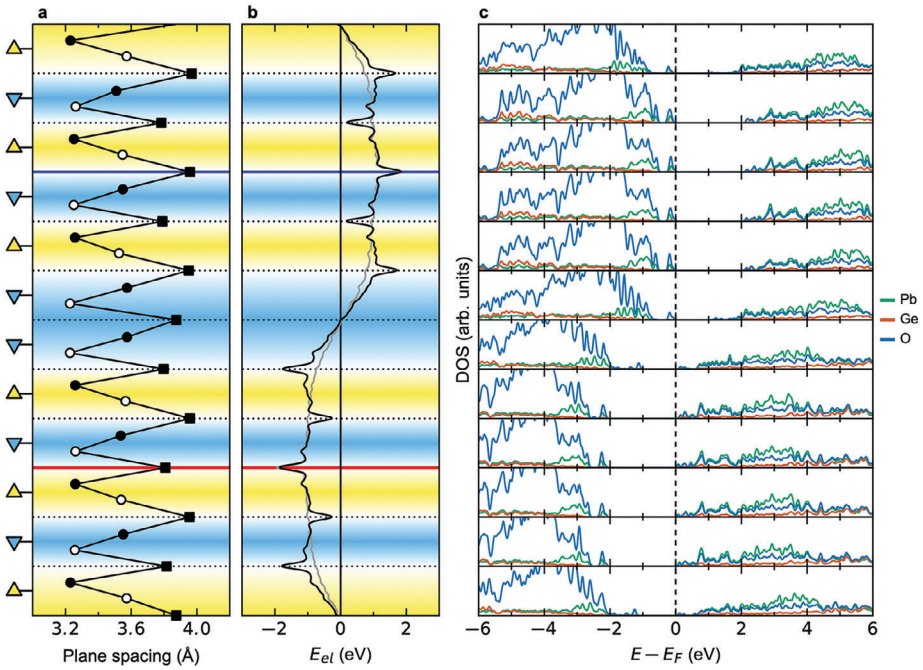

Figure 4. DFT modeling of the antiferroelectric domain wall structure in $Pb_5Ge_3O_{11}$. a–c, Calculated Pb plane spacing (a), local potential profile (b), and electronic density of states (DOS) (c) across the supercell. Yellow and blue arrowheads in a correspond to $+P$ and $-P$ polarizations, respectively, whereas closed circles, open circles, and squares correspond to the plane spacings d_1, d_2, and d_3, respectively. For comparison, the potential for a conventional domain wall configuration (Figure S13, Supporting Information) is plotted in grey in b. The horizontal lines in a and b illustrate positions of interfaces between unit cells of opposite polarization direction, where the red and blue lines mark the center of the charged domain walls. The vertical dashed line in c corresponds to the Fermi level.

directions compared to the upper half, and it is almost identical to the polar Γ_2 mode of the ferroelectric phase (Figure S15c,d, Supporting Information). Thus, one can regard the antiferroelectric phase as a periodic structure, which consists of ferroelectric layers with opposite polarization. We note, however, that the energy lowering associated with the fully relaxed antiferroelectric state (ΔE(AFE) = 3 meV f.u.$^{-1}$) is ≈10 times smaller compared to the energy lowering associated with the ferroelectric (FE) phase (ΔE(FE) = 31 meV f.u. $^{-1}$). Thus, while our DFT calculations show the possibility of competing ferroelectric and antiferroelectric phases in $Pb_5Ge_3O_{11}$, they also show that the antiferroelectric order observed at the domain walls is not the ground state. The latter is corroborated by the calculated domain wall formation energies as a function of domain wall distances in Figure S16 (Supporting Information), which indicates that antiferroelectric domain walls are consistently higher in energy than Ising-type domain walls.

This leads us to the conclusion that the antiferroelectric order observed at the domain walls represents an excited state. Based on domain wall motion seen in Figure 2a–c (as well as Movie S2 and Figures S3 and S4, Supporting Information), the dynamical changes at the unit cell level (Figure S17, Supporting Information), and the reduced ferroelectric distortions measured by ADF STEM (Figure 2d,e), it is reasonable to assume that the excitation is driven by the electron probe. The interaction between electron probe and sample, however, is complex and possible mechanisms include electron-beam-induced heating, beam-induced charging, electric fields and related electrostrictive phenomena, as well as dynamical screening effects. To clarify the physical mechanism, additional in-depth studies are required. Most importantly for this work and the understanding, both theory and experiment indicate that the emergent antiferroelectric order is an excited dynamic state rather than the ground state.

2.5. Electronic domain wall properties

To gain additional insight into the electronic properties of the antiferroelectric domain walls, we model their structure with an antiferroelectric supercell (**Figure** 4a) and calculate the corresponding potential profile (Figure 4b) and local density of states (DOS, Figure 4c) using DFT. The calculations reveal that the antiferroelectric structure leads to a flattening of the electrostatic potential and corresponding band-energy shifts in the DOS compared to individual head-to-head or tail-to-tail domain walls (Figure S18, Supporting Information). Importantly, the results in Figure 4b,c indicate that the conductivity at the antiferroelectric domain walls is similar to the bulk despite the bound charges that exist within the wall (i.e., similar band gap and no additional defect states). The latter is in agreement with previous local transport measurements, which demonstrated that the nominally charged domain walls in $Pb_5Ge_3O_{11}$ exhibit the same electronic conductance as the surrounding domains.[5]

3. Conclusion

The observation of anti-polar order at ferroelectric domain walls extends previous work into the realm of antiferroic phenomena.

In recent years, substantial progress has been made in understanding the properties of bulk antiferroelectrics, reflected by several comprehensive reviews.[24,25] The observation of antiferroelectric order in domain walls, however, is unprecedented both in terms of the effect itself and in terms of the underlying mechanism that relates this phenomenon to competing phonon modes and local electrostatics. Emergence of antiferroelectric order in domain walls represents an extreme example of size effects and thorough investigations are essential for the understanding to the antiferroelectricity. Interestingly, the domain-wall-related evolution from ferroelectric to antiferroelectric order through an aperiodic structure is reminiscent of frustrated magnets. In the latter case, competing magnetic exchange interactions drive the system away from simple ferromagnetic arrangements, promoting incommensurate/aperiodic spin textures and antiferromagnetic order. In particular, the obtained results introduce an innovative strategy for designing antipolar structures, which can be applied also in heterostructures and superlattices: by utilizing hyperferroelectrics in combination with strain and electrostatic boundary conditions – analogous to the conditions found at the charged ferroelectric domain walls – competing polar phases may be exploited to create and fine-tune antiferroelectric 2D systems. This possibility may lead to artificial antiferroelectrics and ferroelectric-antiferroelectric superlattices with unusual physical properties. The engineering of artificial antiferroelectrics and (hyper)ferroelectrics with high-density antiferroelectric domain walls represents a promising approach for increasing the currently limited number of known antiferroelectric single-phase materials and antiferroelectric systems with improved functionality.

4. Experimental Section

Sample Preparation: Electron transparent cross-sections of single crystal $Pb_5Ge_3O_{11}$ were prepared for STEM using a dual-beam focused ion beam (FIB) integrated SEM (Thermo-Fisher Scientific FEI Helios G4 CX). The specimens were mounted onto Omniprobe copper-based lift-out grids. Thinning of the samples was done with decreasing accelerating voltage and electron beam current[26] in four steps: 1) thinning from 2 µm to 800 nm was performed using a 30 keV, 0.23 nA Ga ion beam, 2) 800 to 500 nm: 16 keV, 50 pA, 3) 500 to 300 nm: 8 keV, 50 pA, and 4) below 100 nm: 5 keV, 46 pA. Final polishing was done with 2 keV and 9 pA. Plan view FIB samples were made for STEM imaging of the polar top facet using the method detailed by ref. [27].

Scanning Electron Microscopy: The switching behavior of the domains over large fields of view (i.e., tens of µm) on the surface of the bulk crystal of $Pb_5Ge_3O_{11}$ was analyzed by SEM as shown in Figure S4a,b, (Supporting Information). The data was recorded using a Thermo-Fisher Scientific Apreo SEM with 5 kV acceleration voltage and 0.8 nA electron beam current. See, e.g., ref. [28] for a review on domain and domain wall contrast in SEM. As shown in Figure S4a,b, (Supporting Information), the domain pattern on the non-polar surface changes in every scan, independent of the scan direction of the SEM probe.

Scanning Transmission Electron Microscopy: STEM imaging was performed using a Thermo-Fisher Scientific double aberration-corrected monochromated Titan Themis Z, operated at 300 kV accelerating voltage. The convergence angle for ADF STEM imaging was 24 mrad and the collection angle was 52–200 mrad using the HAADF detector; the measured fluorescent screen current was ≈30 pA. Additional imaging was carried out using a Nion UltraSTEM 100MC "Hermes" microscope at a lower accelerating voltage of 60 kV, with a convergence semi-angle of 33 mrad and typical beam current of 30pA. The HAADF detector angular range was 85–180 mrad. STEM DPC mapping was done using a segmented ADF detector and processed via Thermo-Fisher Velox software. To capture the internal atomic-scale structure, initially a domain wall was imaged using low magnification STEM DPC. After several scans from the same direction, a charged domain wall became stable. Then the beam was blanked, and the magnification was increased to the required level with enough pixels per atomic column for post-processing. After this, a single STEM ADF frame was captured. The presence of the domain wall pattern was readily identified by respective extra spots in the Fourier transform of the STEM image, which arise due to the alternating direction of Pb atoms displacement at the unit cell level (Figure S11, Supporting Information). If a longer camera length (and thus decreased collection angle) was used for ADF imaging, the domain wall was seen as an alternating stripe of high and low contrast, associated with the changing in the atomic column spacing as seen in Figure 3a–c. Series of consecutive STEM images with relatively short pixel dwell times were drift-corrected by first aligning and averaging all images in a time series and then calculating a mean unit cell. Next, this unit cell was tiled to fill the entire image, which was then used as a reference image for measuring and correcting the distortions using the procedure given in ref. [29] Since absolute distances were not preserved, only relative site displacements were measured. To analyze the $Pb_5Ge_3O_{11}$ structure, the images both in one dimension (1D) perpendicular to the domain wall and in two dimensions (2D) were averaged, to produce mean unit cells as described by Danaie et al..[30] This averaging was performed by first fitting the peak positions and then assigning each peak to a lattice coordinate, and finally computing the best fit lattice. In the 1D and 2D averaged images, we fit each Pb site to a 2D Gaussian distribution to estimate its position. For the displacement plots shown in Figure 2, the total unit cell dimensions were equal to the bulk value were assumed. Transmission electron microscopy (TEM) using parallel beam mode and the Gatan Oneview camera were used to suppress effects from domain wall motion during imaging. The response of the sample, however, was dose-rate dependent and the threshold value was found to be too low to achieve atomic resolution, so that STEM imaging was performed instead. Dose measurements were acquired by taking the reading from the incident beam hitting the fluorescent screen in units of e^- Å^{-2}, which was converted into a dose rate based on the exposure time of acquisition. The Pb–Pb plane spacing (i.e., d_1, d_2, and d_3) was estimated from 14 unit cells of the $-P$ domain shown in Figure 3d, with the error bars representing the standard deviation of these measurements.

Density Functional Theory: Density functional theory calculations were performed using VASP.[31–33] The domain walls were modeled by 684 atom supercells comprised of 12 unit cells along the lattice vector c. Since the domain walls were experimentally found to span far beyond what our DFT models can capture, two unit cells in each domain were fixed to the relaxed bulk structure to ensure bulk-like properties in the center of each domain. The domain walls were modeled by four unit cells accordingly. Pb (5d, 6s, 6p), Ge (3d, 4s, 4p), and O (2s, 2p) were treated as valence electrons, with a plane-wave cutoff energy of 550 eV. Brillouin zone integration was performed using a Γ-centered 2 × 2 × 2 grid for unit cell calculations, and a 2 × 2 × 1 grid for the charged domain wall supercells. Lattice positions were relaxed until the residual forces on all the atoms were below 0.05 eV Å^{-1}, with lattice parameters fixed to relaxed bulk values. Ferroelectric polarization was determined using the Berry phase method,[34–36] performed on unit cells extracted from the relaxed domain wall supercells. Frozen phonon calculations[37] were performed on 2 × 2 × 2 supercells (456 atoms) with the finite displacement method as implemented in the PHONOPY code,[38] using atomic displacements of 0.01 Å for calculating the force constants. Phonon analysis was carried out using the AMPLIMODES[6] and Sumo[39] packages.

Supporting Information

Supporting Information is available from the Wiley Online Library or from the author.

Acknowledgements

M.C. acknowledges funding from Science Foundation Ireland (SFI) Industry Fellowship (18/IF/6282), Royal Society Tata University Research Fellowship (URF\R1\201318), EPSRC NAME Programme Grant EP/V001914/1 and Royal Society Enhancement Award RF\ERE\210200EM1. The research by M.C., K.M., J.M.G., U.B., and A.G. was supported by the US-Ireland R&D Partnership Programme (grant no. USI 120), National Science Foundation (NSF) grant DMR-1709237 and Science Foundation Ireland (16/US/3344). D.R.S. and S.M.S. acknowledge the Research Council of Norway (FRINATEK project No. 275139/F20) for financial support. D.R.S. and U.A. acknowledge the Swiss National Science Foundation (Project No. 200021_178791) for financial support. Computational resources were provided by UNINETT Sigma2 (project no. NN9259K), and UBELIX (http://www.id.unibe.ch/hpc) – the HPC cluster at the University of Bern. C.O. acknowledges support from the DOE Early Career Research Program. Work at the Molecular Foundry was supported by the Office of Science, Office of Basic Energy Sciences, of the U.S. Department of Energy under Contract No. DE-AC02-05CH11231. SuperSTEM is the U.K. National Research Facility for Advanced Electron Microscopy, supported by the EPSRC through grant EP/W021080/1. M.S. and K.S. acknowledge support from Ministerio de Ciencia Y Innovación (MICINN-Spain) through Grant No. PID2019-108573GB-C22; from the State Investigation Agency through the Severo Ochoa Programme for Centres of Excellence in R&D (CEX2023-001263-S); from Generalitat de Catalunya (Grant No. 2021 SGR 01519); and from the European Research Council (Grant Agreement No. 724529). D.M. thanks NTNU for support through the Onsager Fellowship Program, the Outstanding Academic Fellow Program, and acknowledges funding from the European Research Council (ERC) under the European Union's Horizon 2020 Research and Innovation Program (Grant Agreement No. 863691). The Research Council of Norway (RCN) is acknowledged for the support to the Norwegian Micro- and Nano-Fabrication Facility, NorFab, project number 295864.

Conflict of Interest

The authors declare no conflict of interest.

Author Contributions

M.C., D.R.S., and C.O. contributed equally to this work. M.C. prepared the FIB samples. STEM measurements were performed by M.C., with advice from C.O. and Q.R.; D.R.S. carried out DFT calculations supervised by S.M.S. and U.A. M.C. and C.O. performed STEM data analysis. K.A.H. performed SEM measurements and contributed to the basic structure analysis, supervised by D.M. and K.S. analyzed the DFT results and the antiferroelectric ordering supervised by M.S. and J.M.G. analyzed the domain wall structure. D.M. and A.G. initiated and coordinated the project and wrote the manuscript together with M.C. and D.R.S. and with input from all authors. All authors discussed the results and contributed to the final version of the manuscript.

Data Availability Statement

The data that support the findings of this study are available from the corresponding author upon reasonable request.

Keywords

antiferroelectric, DFT calculations, domain wall, scanning transmission electron microscopy

Received: April 10, 2024
Revised: July 6, 2024
Published online:

[1] S. Nanamatsu, H. Sugiyama, K. Doi, Y. Kondo, *J. Phys. Soc. Jpn.* **1971**, *31*, 616.
[2] H. Iwasaki, K. Sugii, *Appl. Phys. Lett.* **1971**, *19*, 92.
[3] A. Gruverman, N. Ponomarev, K. Takahashi, *Jpn. J. Appl. Phys.* **1994**, *33*, 5536.
[4] Y. Tikhonov, J. R. Maguire, C. J. McCluskey, J. P. V. McConville, A. Kumar, H. Lu, D. Meier, A. Razumnaya, J. M. Gregg, A. Gruverman, V. M. Vinokur, I. Luk'yanchuk, *Adv. Mater.* **2022**, *34*, 2203028.
[5] O. Bak, T. S. Holstad, Y. Tan, H. Lu, D. M. Evans, K. A. Hunnestad, B. Wang, J. P. V. McConville, P. Becker, L. Bohatý, I. Lukyanchuk, V. M. Vinokur, A. T. J. van Helvoort, J. M. Gregg, L.-Q. Chen, D. Meier, A. Gruverman, *Adv. Funct. Mater.* **2020**, *30*, 2000284.
[6] D. Orobengoa, C. Capillas, M. I. Aroyo, J. M. Perez-Mato, *J. Appl. Crystallogr.* **2009**, *42*, 820.
[7] V. I. Dvořák, *Ferroelectrics* **1974**, *7*, 1.
[8] A. P. Levanyuk, G. S. Daniil, *Phys.-Usp.* **1974**, *17*, 199.
[9] M. Stengel, N. A. Spaldin, D. Vanderbilt, *Nat. Phys.* **2009**, *5*, 304.
[10] K. F. Garrity, K. M. Rabe, D. Vanderbilt, *Phys. Rev. Lett.* **2014**, *112*, 127601.
[11] M. Fava, W. Lafargue-Dit-Hauret, A. H. Romero, E. Bousquet, *Phys. Rev. B* **2023**, *108*, L201112.
[12] M. Fava, W. Lafargue-Dit-Hauret, A. H. Romero, E. Bousquet, *Phys. Rev. B* **2024**, *109*, 024113.
[13] S. Liu, R. Cohen, *J. Phys.: Condens. Matter* **2017**, *29*, 244003.
[14] H. J. Zhao, A. Filippetti, C. Escorihuela-Sayalero, P. Delugas, E. Canadell, L. Bellaiche, V. Fiorentini, J. Íñiguez, *Phys. Rev. B* **2018**, *97*, 054107.
[15] M. Campanini, M. Trassin, C. Ederer, R. Erni, M. D. Rossell, *ACS Appl. Electron. Mater.* **2019**, *1*, 9186.
[16] M. Conroy, K. Moore, E. O'Connell, L. Jones, C. Downing, R. Whamore, A. Gruverman, M. Gregg, U. Bangert, *Microsc. Microanal.* **2020**, *26*, 3030.
[17] A. Lubk, J. Zweck, *Phys. Rev. A* **2015**, *91*, 023805.
[18] K. Moore, M. Conroy, E. N. O'Connell, C. Cochard, J. Mackel, A. Harvey, T. E. Hooper, A. J. Bell, J. M. Gregg, U. Bangert, *Commun. Phys.* **2020**, *3*, 231.
[19] M. Barzilay, Y. Ivry, *Nanoscale* **2020**, *12*, 11136.
[20] M. I. Kay, R. E. Newnham, R. W. Wolfe, *Ferroelectrics* **1975**, *9*, 1.
[21] C.-L. Jia, S.-B. Mi, K. Urban, I. Vrejoiu, M. Alexe, D. Hesse, *Nat. Mater.* **2008**, *7*, 57.
[22] J. Gonnissen, D. Batuk, G. F. Nataf, L. Jones, A. M. Abakumov, S. Van Aert, D. Schryvers, E. K. H. Salje, *Adv. Funct. Mater.* **2016**, *26*, 7599.
[23] K. Moore, M. Conroy, U. Bangert, *J. Microsc.* **2020**, *279*, 222.
[24] Y. Si, T. Zhang, C. Liu, S. Das, B. Xu, R. G. Burkovsky, X.-K. Wei, Z. Chen, *Prog. Mater. Sci.* **2024**, *142*, 101231.
[25] S. Chen, S. Yuan, Z. Hou, Y. Tang, J. Zhang, T. Wang, K. Li, W. Zhao, X. Liu, L. Chen, L. W. Martin, Z. Chen, *Adv. Mater.* **2021**, *33*, 2000857.
[26] M. Schaffer, B. Schaffer, Q. Ramasse, *Ultramicroscopy* **2012**, *114*, 62.
[27] C. Li, G. Habler, L. C. Baldwin, R. Abart, *Ultramicroscopy* **2018**, *184*, 310.
[28] K. A. Hunnestad, E. D. Roede, A. T. J. Van Helvoort, D. Meier, *J. Appl. Phys.* **2020**, *128*, 191102.
[29] C. Ophus, J. Ciston, C. T. Nelson, *Ultramicroscopy* **2016**, *162*, 1.
[30] M. Danaie, D. Kepaptsoglou, Q. M. Ramasse, C. Ophus, K. R. Whittle, S. M. Lawson, S. Pedrazzini, N. P. Young, P. A. J. Bagot, P. D. Edmondson, *Inorg. Chem.* **2016**, *55*, 9937.
[31] P. E. Blöchl, *Phys. Rev. B: Condens. Matter Mater. Phys.* **1994**, *50*, 17953.
[32] G. Kresse, J. Furthmüller, *Phys. Rev. B: Condens. Matter Mater. Phys.* **1996**, *54*, 11169.

[33] G. Kresse, D. Joubert, *Phys. Rev. B* **1999**, *59*, 1758.
[34] R. D. King-Smith, D. Vanderbilt, *Phys. Rev. B* **1993**, *47*, 1651.
[35] R. Resta, *Rev. Mod. Phys.* **1994**, *66*, 899.
[36] N. A. Spaldin, *J. Solid State Chem.* **2012**, *195*, 2.
[37] K. Kunc, R. M. Martin, *Phys. Rev. Lett.* **1982**, *48*, 406.
[38] A. Togo, I. Tanaka, *Scr. Mater.* **2015**, *108*, 1.
[39] A. M. Ganose, A. J. Jackson, D. O. Scanlon, *J. Open Source Software* **2018**, *3*, 717.